CFD-guided patterning of tubular ceramic membrane surface by stereolithograhy: Optimizing morphology at the mesoscale for improved hydrodynamic control of membrane fouling

Cyril Chevarin[1], Xunhao Wang[2], Denis Bouyer[1*], Volodymyr Tarabara[2**], Thierry Chartier[3], André Ayral[1]

[1] *Institut Européen des Membranes IEM – UMR 5635, ENSCM, CNRS, Univ Montpellier, Montpellier, France*

[2] *Department of Civil and Environmental Engineering, Michigan State University, East Lansing, MI 48824, USA*

[3] *CNRS, University of Limoges, Institute of Research for Ceramics (IRCER), UMR 7315, European Ceramics Center, Limoges, France*

Abstract

A preliminary study was carried out on the morphological design of tubular single-channel alumina membranes prepared by stereolithography, an additive manufacturing process. The geometry of the ring-patterned inner surface of membranes was optimized using computational fluid dynamics calculations and validated in microfiltration tests with aqueous suspensions of *P. aeruginosa*. Patterning of the inner surface of tubular membranes helped reduce cake formation at a higher value of the average crossflow velocity. The results highlight benefits of stereolithography-based approach to the morphological design of ceramic membranes.

Keywords: ceramic membrane, computational fluid dynamics, stereolithography, fouling

* Corresponding author. *Institut Européen des Membranes, Univ Montpellier, Montpellier, France*

** Corresponding author. *Department of Civil and Environmental Engineering, Michigan State University, East Lansing, USA*

E-mail addresses: denis.bouyer@umontpellier.fr (D. Bouyer), tarabara@msu.edu (V. V. Tarabara).

1. Introduction

Rapid advances in additive manufacturing have paved the way for the simplified fabrication of integrated systems as well as system components with complex shapes hitherto inaccessible by conventional manufacturing methods. It is particularly the case for ceramic materials [1-3], which require high temperature sintering to confer morphological, microstructural and mechanical properties to the shaped object. These advances open up new possibilities for the design of ceramic membranes. Indeed, there is a growing interest in the use of additive manufacturing methods to prepare both membranes, including ceramic filters [4-6], and membrane modules [7-11].

Many of the current membrane processes are based on the principle of crossflow filtration, with key concerns regarding the minimization of concentration polarization and fouling. Fouling management often requires a regular interruption of the filtration process by cleaning sequences (e. g. backwashing) limits the lifetime of the membranes. A complementary approach to minimizing fouling and its deleterious effects is to promote turbulence in the feed flow. The use of turbulence promoters is possible but at a cost of an increased pressure drop in the feed flow channel. Another option is to promote turbulence closer to the membrane surface by altering its topography. This has been the subject of various studies, most of which focused on the surface patterning of polymer membranes [12-14] although some did employ flat plate ceramic membranes [15, 16].

Most installations use ceramic membranes in a tubular configuration, the support of which is produced by extrusion. Based on a computational fluid dynamics (CFD) approach, Yang et al. explored optimization of multi-channel ceramic membranes [17]. While the number and the section of the channels are easily adjustable, the same cannot be said for their surface morphology. Twenty years ago a clever method was developed, allowing the extrusion of tubular supports with a spiral internal surface favoring the turbulence of the flow [18]. During the 2018 International Conference in Inorganic Membranes, a presentation by TAMI Industries highlighted the CFD-based prediction of the benefits of having curvilinear flow inside a tubular membrane channel, the practical implementation of such flow field using bundles of helical membranes, as well as the potential of additive processes for manufacturing such membranes [19].

The present work concerns a preliminary study on the morphological design of ceramic tubular membranes. Single-channel alumina tubular membranes with an inner diameter of 7 mm and an outer diameter of 10 mm were selected, corresponding to usual specifications for current commercial membranes of this type. The inner surface the membrane was patterned with rings – morphological elements that cannot be introduced at the membrane surface by the conventional shaping method based on paste extrusion. The ring profile and height as well as the inter-ring distance were optimized using CFD modeling by evaluating the impact of these parameters on the turbulence near the membrane surface. CFD predictions were validated in preliminary experiments with symmetric alumina microfiltration (pore diameter of ~ 0.2 µm) membranes, with or without such rings, manufactured by an additive process (i. e. stereolithography) from alpha alumina powder. The patterned membranes and smooth membranes (controls) were comparatively evaluated in terms of fouling behavior in experiments with *P. aeruginosa.* suspensions.

2. Numerical model

2.1. Geometry

The flow hydrodynamics in the tubular membranes was simulated for both smooth and patterned membranes as shown in Figure 1. Here, “patterned” refers to a membrane with the inner (feed-facing) surface having a patterned morphology. In both configurations (smooth or patterned inner surface), the outer diameter and the membrane length were 10 mm and 50 mm, respectively. The inner diameter of both membranes was 7 mm everywhere except in locations corresponding to roughness elements (“rings”) on the surface of the patterned membrane; each such “ring” was ~ 0.5 mm high, leading to a somewhat smaller inner diameter in those locations. Thanks to the axial symmetry, simulations were performed using 2D axisymmetric geometry thus notably reducing the calculation time.

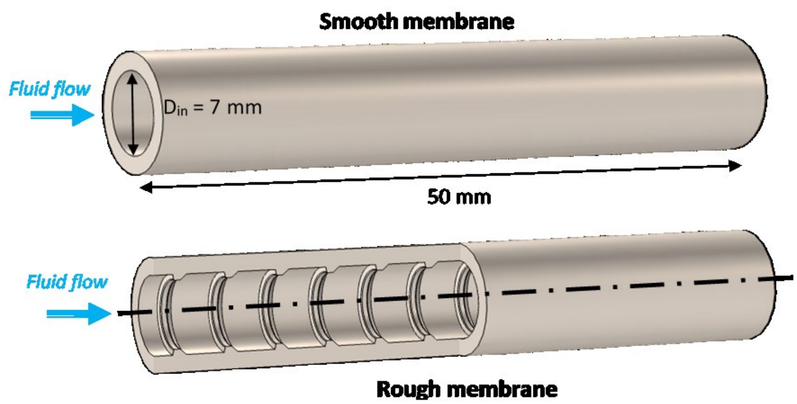

Figure 1. Geometry of smooth and patterned tubular membranes.

2.2. Governing equations

Two feed flow rates were simulated herein, with mean velocities of 0.45 m·s^{-1} and 0.68 m·s^{-1}, respectively in agreement with the values used in filtration experiments. These values are within the typical range of crossflow velocities employed in tangential filtration applications (e. g. [20]) although for ultra- and microfiltration with ceramic membranes crossflow velocities may be significantly higher – up to 4 m/s [21]. Given the density and viscosity of water at 23 °C, the diameter of the flow channel, and the two mean velocities, Reynolds numbers of 3100 and 4830, respectively were calculated, corresponding to the end of the transition zone between laminar and turbulent hydrodynamic regimes. Consequently, the classical Reynolds Averaged Navier–Stokes (RANS) transport equations for incompressible Newtonian fluid and turbulent regime were used in the model.

In the RANS model, the conservation of momentum equation is given by:

$$\rho(\nabla.\vec{v})\vec{v} = -\nabla p + \nabla.\left((\eta + \eta_t)[(\nabla\vec{v} + \nabla\,\vec{v}^T)]\right) + \rho\vec{g} \quad (1)$$

where ρ is the water bulk density (kg.m^{-3}), $\vec{v}$ is the velocity vector (m.s^{-1}), p is the static pressure (Pa), $[(\nabla\vec{v} + \nabla\,\vec{v}^T)] = \acute{t}$ is the viscous stress tensor, η is the dynamic viscosity of the water (Pa.s), η_t is the turbulent (or eddy) viscosity (Pa.s) and $\vec{g}$ is the acceleration due to gravity (m.s^{-2}).

The standard k-ε model [22] (see Supplementary Information (SI), section S1) was used to simulate the turbulence, meaning that the turbulent viscosity η_t was modeled using eq. (2) [23]:

$$\eta_t = \rho C_\eta \frac{k^2}{\varepsilon}, \quad (2)$$

where C_η is a constant, k is the turbulent kinetic energy (m^2.s^{-2}) and ε is the turbulent energy dissipation rate (m^2.s^{-3}).

2.3. Boundary conditions

Fully developed flow with a mean velocity (in m.s^{-1}) was considered in the model for boundary conditions in the inlet side. Two mean velocities were simulated, i. e. 0.45 m.s^{-1} and 0.68 m.s^{-1}. At the outlet side, a null static pressure boundary condition P_0 was fixed. A no-slip boundary condition was applied at the wall.

2.4. Numerical simulations

The hydrodynamic model was simulated using the commercial COMSOL Multiphysics® software, working with finite element method. Using a 2D axis-symmetric model, meshes size was ranged between 0.08 mm near the wall and 0.2 mm in the bulk of the flow. Boundaries layers and finer meshes were built near the wall surfaces to improve the numerical accuracy in the boundary layer. The number of tetrahedral meshes was close to 100 000 for the simulations without rings and 140 000 for the simulations with rings.

3. Experimental

3.1. Membrane manufacturing and microstructural characterization

The membranes were manufactured by the company 3DCERAM SINTO (Limoges, France) according to our specifications. The green bodies were built using the stereolithography additive process (CERAMAKER 900 machine) based on the selective polymerization of a reactive mixture system under the effect of a UV irradiation. The reactive system was a suspension of alumina particles (1.75 µm mean particle size) in a mixture of curable monomer and oligomer, with the addition of a photoinitiator. For more details on stereolithography-based processing of ceramic components, please refer to the chapter on the topic by Chartier and Badey [1].

After debinding and sintering, the pieces were externally machined to achieve the requested dimensional specifications (outer diameter = 10.0 ± 0.2 mm; inner diameter = 7.0 ± 0.2 mm; length = 49.2 ± 0.2 mm). Taking into account the applied sintering conditions (maximal temperature larger than 1200°C) and the nature of the used ceramic powder (i. e. pure alpha alumina), excellent stability of the membrane microstructure can be expected even for long exposure to aqueous media. The experimentally observed stability of membrane permeability with time is consistent with this expectation.

For the patterned membranes, the targeted characteristics for rings were as follows: height of 500 µm; a the upstream and the downstream edges forming an angle of 80° and 135°, respectively, with the direction of the flow, and the 3mm distance between two neighboring rings. The geometry of the patterned membranes was confirmed by making a cutout in one of these tubes using a diamond saw, observing this sample by Keyence VHX 6000 digital microscope (VHX) and then analyzing the Keyence images with suitable image processing software (VHX-6000_950F).

The microstructure of the membranes was investigated using a Field Emission Scanning Electron Microscope (FE-SEM; Hitachi S4800). The porosity of these macroporous samples was determined by mercury porosimetry (AutoPore IV 9500 Micromeritics).

3.2. Fouling experiments

3.2.1. Experimental setup and membrane permeability measurements

The membranes were tested using a crossflow filtration system (see SI, Figure S1), which included a peristaltic pump (910-0025, Thermo Scientific), a custom-made membrane unit and a back-pressure valve (SS-43S6, Swagelok). The membrane was mounted using two stainless steel push-to-connect fittings (KQG2H10-00, Grainger). To seal the membrane area under the fittings and ensure it is not available for permeation, the outside surface of the membrane under the fittings was coated with a thin layer of epoxy (LOCTITE, Henkel). The pure water flux tests for the 3D-printed membranes were performed using DI water and five different transmembrane pressure values: 1.03, 1.38, 1.72, 2.07, and 2.41 bar (15, 20, 25, 30, and 35 psi, respectively). The DI water (pH 5.8) was used as the feed solution in these tests. The crossflow velocity was maintained constant at either 0.45 $m{\cdot}s^{-1}$ or 0.68 $m{\cdot}s^{-1}$. The permeability of each membrane was calculated based on the slope of the flux vs pressure dependence.

3.2.2. Bacterial suspensions: Preparation and characterization

An aqueous suspension of *P. aeruginosa* (Schroeter) Migula (PA01-LAC, ATCC) was used as the feed in membrane fouling tests. *P. aeruginosa* were cultured in Luria-Bertani (LB) broth to the exponential growth phase. The standard curve (colony-forming units per milliliter (CFU/ml) vs absorbance at 600 nm) was established. The preparation of the bacteria stock is detailed in the SI file, section S2. The bacteria were enumerated by a colony count method. Briefly, the vortexed solutions were serially diluted, mixed with soft agar, and poured onto LB-agar plates, which were incubated at 37 °C overnight. The formed colonies were counted, and then the areal density of colony-forming units (CFU/ml) was calculated. The absorbance of the bacterial suspensions was measured by a spectrophotometer (Spectronic 21D). The hydrodynamic diameter of bacteria was measured by dynamic light scattering (DLS). In these tests, a small sample (0.5 mL) of the bacterial suspension was diluted in 1 mM KCL solution, prefiltered with 0.22 µm syringe filter, to the total volume of ~ 2 mL.

3.2.3. Membrane fouling tests

Prior to each crossflow filtration test, the feed suspension was prepared by diluting the bacteria stock ten-fold with DI water. The volume fraction of *P. aeruginosa* in the feed was $3.9\ 10^{-5}$. With the elliptical shape and the size range for *P. aeruginosa* [24] taken into account, this volume fraction translates into the number-based concentration in the range from $3.9{\times}10^{7}$ to $19.9{\times}10^{7}$ bacteria/mL. Based on this low value of the volume fraction and the Einstein relation between relative viscosity and volume fraction of dispersed phase [25], the viscosity of this suspension was considered to be equal to that of pure water. The ionic strength of the feed was 15 mM. During fouling tests, the crossflow velocity (averaged across the membrane channel cross-section) was 0.45 $m{\cdot}s^{-1}$ or 0.68 $m{\cdot}s^{-1}$, which corresponded to the maximum crossflow rate (1570 $mL{\cdot}min^{-1}$) that the peristaltic pump could provide at the transmembrane pressure used in the tests (30 psi; ~ 2.1 bar). The scope of the present study was limited to the specific values of the crossflow velocity and the transmembrane pressure that were employed experimentally and matched in CFD simulations. While the values assessed herein are typical, some applications (e. g. with unusually high recoveries) would require additional testing and modeling to better understand how the patterned morphology affects membrane performance under those conditions.

Prior to challenging the membrane with the bacterial suspension, the membrane was equilibrated with 15 mM NaCl at pH 6. The permeate was collected on a mass balance with a 1 min interval. All fouling tests were done at the ambient temperature of 23 °C and the relative humidity of 47%. After each fouling test, the membrane was cleaned by circulating solutions in the feed channel in the following sequence: (1) DI water for 30 min, (2) 5 mM EDTA at pH 11 for 30min, (3) DI water for 30 min, (4) 2 mM SDS at pH 11 for 30 min, (5) DI water for 30 min [26].

Three smooth and three patterned membranes were tested under the same experimental conditions to estimate the reproducibility of the results. In order to investigate the contribution of the different fouling mechanisms to the overall decline in permeate flux, additional tests were carried out in the dead-end filtration regime following a procedure described earlier [27].

4. Results and discussion

4.1. Membrane design from numerical simulations

As mentioned in the introduction, in the frame of this pioneering study, it was decided to pattern the inner surface of the tubular membranes with simple and continuous rings. The current limitations of the existing additive manufacturing in terms of dimensional tolerances were considered for sizing these rings. The dimensional resolution afforded by stereolithography is ~ 100 µm [2]. Due to the concern that features approaching this size scale might lose in fidelity and in feature-to-feature consistency, the ring height was chosen to be 500 µm as features of this size could be made using stereolithography with good precision. With regard to rings of a larger size, one can expects that increasing the ring height would be disadvantageous in terms of the distribution of ε, likely leading to large dead zones. The above considerations led to the decision to prepare rings with a height and a width of 500 µm.

Moreover, using the CFD model we investigated the influence of the inter-ring distance as it changed from 3 to 5 mm. The results are shown in SI. Simulations for an inter-ring distance of 2 mm were also performed and they exhibited the most interesting results in terms of the spatial distribution of turbulent kinetic energy ε. While stereolithography does allow to prepare patterned membranes with this lower inter-ring distance (2 mm), the process becomes more complex due to the difficulty of removing the unpolymerized paste after manufacturing and before debinding/sintering. This is the reason why the smallest inter-ring distance evaluated experimentally was 3 mm.

Figures 2 and 3 show the spatial distribution of the dissipation rate of turbulent kinetic energy, ε, in three different configurations (smooth membrane, patterned membrane featuring rings with symmetrical profile, patterned membrane featuring rings with asymmetrical profile), for average inlet velocities of 0.45 and 0.68 $m \cdot s^{-1}$, respectively.

Whatever the configuration, ε is much higher close to the top of the rings compared to the region between the rings, with a ratio close to 23 at 0.45 $m \cdot s^{-1}$ and more than 42 at 0.68 $m \cdot s^{-1}$. A 50% increase in the inlet velocity (from 0.45 to 0.68 $m \cdot s^{-1}$), leads to a five-fold increase in ε at the top of the rings and a three-fold increase in ε between the rings. These results confirm the intuitive predictions, highlighting the interest to disturb the flow near the membrane surface to create more turbulence (more dissipation of turbulent kinetic energy). With this geometrical configuration, the risk lies in the formation of dead zone between the rings that is the zone with local re-circulation and characterized by a lower level of turbulence. Further, when analyzing the influence of the ring shape (symmetric vs asymmetric), the numerical simulations clearly show that the low ε region, localized just downstream of each ring, is smaller behind rings with the asymmetrical profile. For both inlet velocities evaluated (0.45 or 0.68 $m \cdot s^{-1}$), asymmetry appears to be favorable for preventing fouling phenomena. Based on these numerical results, the asymmetric profile was selected.

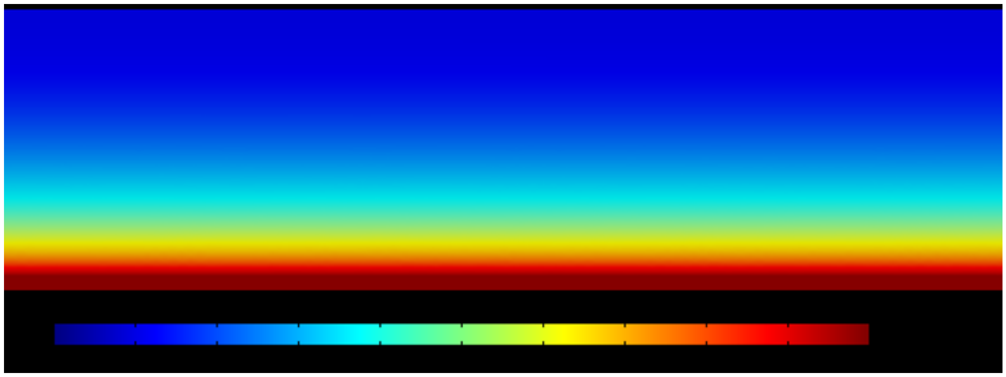

(a) Smooth membrane

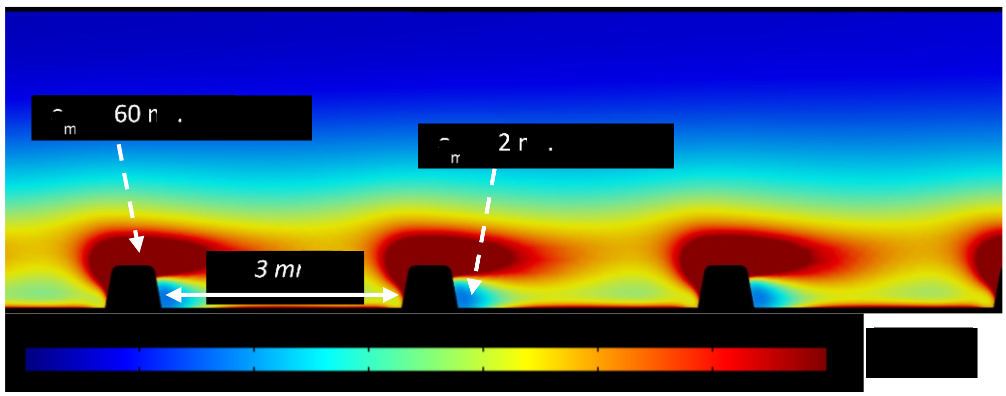

(b) Patterned membrane – symmetrical profile of surface “rings”

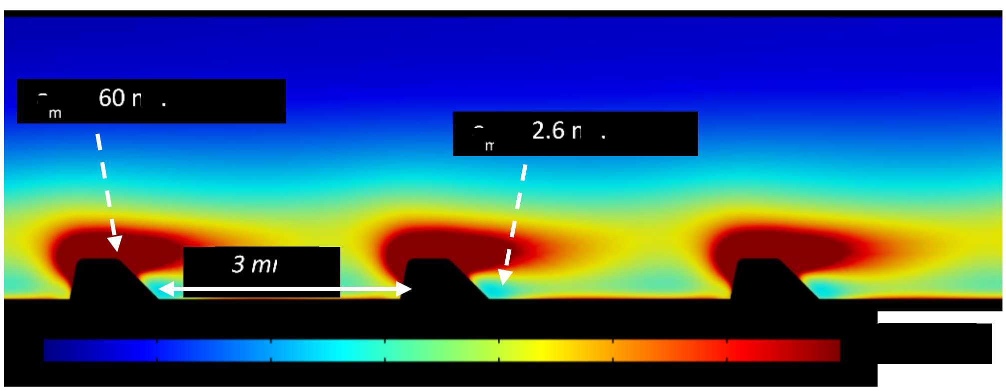

(c) Patterned membrane – asymmetrical profile of surface “rings”

Figure 2. Dissipation rate of turbulent kinetic energy, ε, in the vicinity of the rings on the surface of the tubular membrane for v_{in}= 0.45 m·s^{-1}: (a) smooth membrane, (b) patterned membrane featuring “rings” with symmetrical profile*, (c) patterned membrane featuring “rings” with asymmetrical profile.*

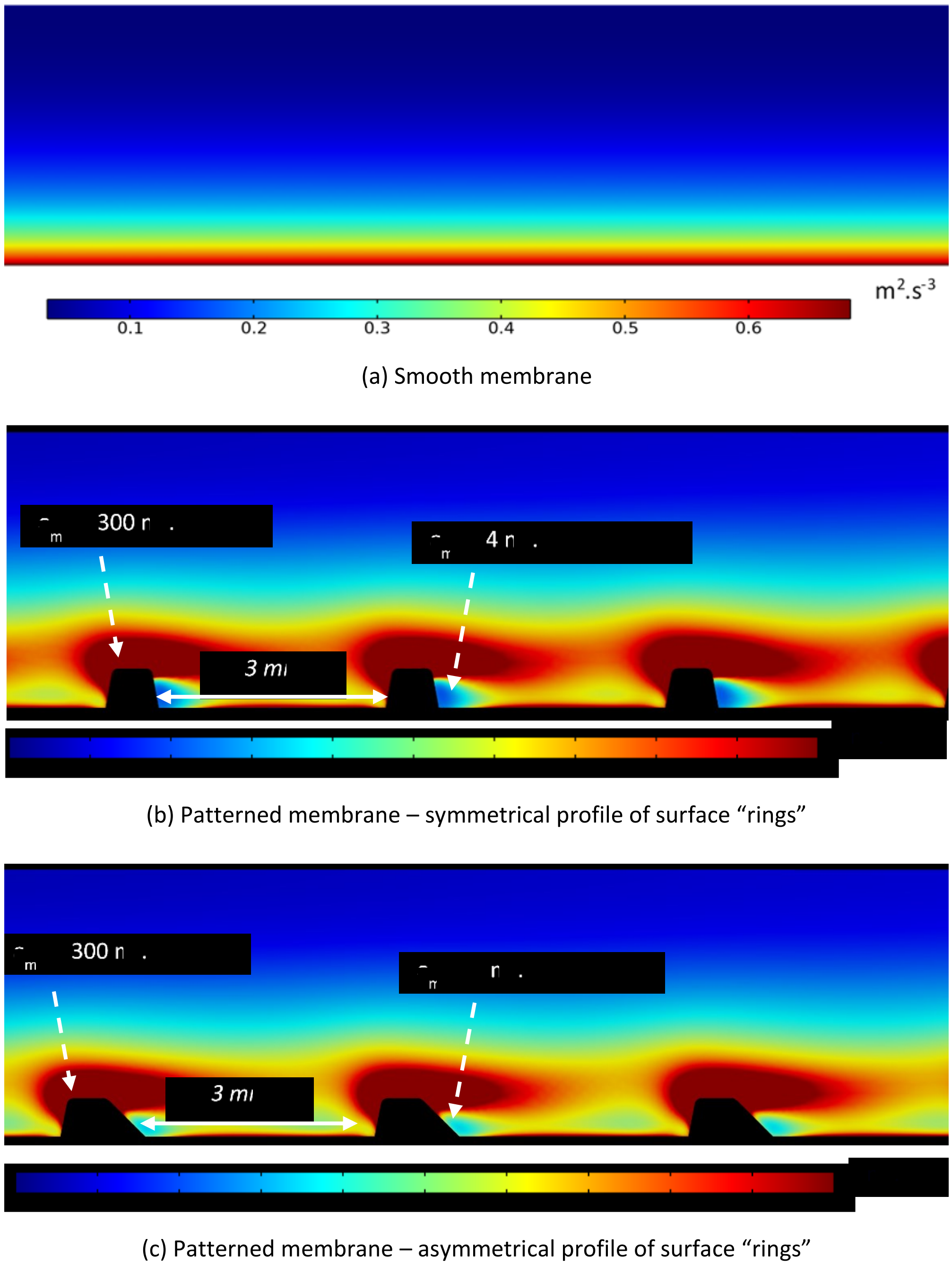

Figure 3. Dissipation rate of turbulent kinetic energy, ε, in the vicinity the rings on the surface of the tubular membrane for v_{in}= 0.68 m·s^{-1}: (a) smooth membrane, (b) patterned membrane featuring “rings” with symmetrical profile*, (c) patterned membrane featuring surface “rings” with asymmetrical profile.*

Preliminary CFD study of the impact of the inter-ring distance (see SI, Figure S2) showed that it had a relatively minor effect on the spatial distribution of ε. As a result of this assessment, the inter-ring distance of 3 mm was selected as allowing the highest reduction in the spatial extent of low ε zones. Simulations pointed out the interplay between the ring shape (symmetric vs asymmetric) and the inlet velocity as both affected the spatial distribution of ε: for an inlet velocity of 0.68 m·s^{-1}, the low ε value is increased by 75% (7 m^2·s^{-3} vs 4 m^2·s^{-3}) when using the asymmetric rings, while it is only increased by 30% when the inlet velocity is equal to 0.45 m·s^{-1}.

Table 1 summarizes the values of the energy dissipation rate ε and the pressure loss along the membrane. These values give an indication of the cost of integrating the rings as turbulence promoters within the tubular membrane. Whatever the inlet velocity, the pressure loss increases by a factor 15 when using patterned membranes rather than smooth ones. This result is not surprising because it is directly linked to the total dissipation rate of turbulent kinetic energy, and it should be related to the energy cost of back-washing frequency that should be done between two filtration cycles.

Table 1. Specific pressure loss, ΔP_{feed}, in the feed flow along the membrane and mean value of turbulent dissipation rate, ε_{mean}, at the membrane surface for two values of the average crossflow velocity, v_{in}. Turbulent dissipation rate is for the membrane surface between the rings and is deduced from the simulations graphically represented in Figure S2.

	Smooth membrane		Patterned membrane	
	v_{in} = 0.45 m·s^{-1}	v_{in} = 0.68 m·s^{-1}	v_{in}= 0.45 m·s^{-1}	v_{in}= 0.68 m·s^{-1}
ε_{mean} (m^2·s^{-3})	0.10	0.45	4.6	16.3
ΔP_{feed} (bar·m^{-1})	0.006	0.013	0.092	0.204

Table 1 shows that a significant advantage can be expected with the patterned membranes in terms of fouling limitation, especially for the largest value of average inlet crossflow velocity. The reported values of specific pressure loss in the feed flow qualitatively account for the additional energy cost associated with the use of patterned membranes. The determined values are more than one order of magnitude larger for the patterned membranes but rather low in absolute value.

4.2. Microstructural characterization of the manufactured membranes

Figure 4 shows the internal morphology of the patterned membranes with the axisymmetric structure of the roughness elements (“rings”) clearly shown (Figure 4a). The ring profile (Figure 4b) and the inter-ring spacing (Figure 4c) correspond rather well to the targeted characteristics considering the 100 µm spatial resolution of the implemented additive method. SEM imaging of the planar surface (Figure 5a) and the cross-section (Figure 5b) of the membranes showed a close packing arrangement of grains with a bimodal size distribution. The continuous matrix with submicron grains (~0.6 µm in size) is embedded with larger grains several microns in size. One can expect the pore size to be approximately one third of the grains’ size. The reported pore size of 0.2 µm is indeed 3 times smaller than the grain size of the submicronic fraction of the bimodal distribution.

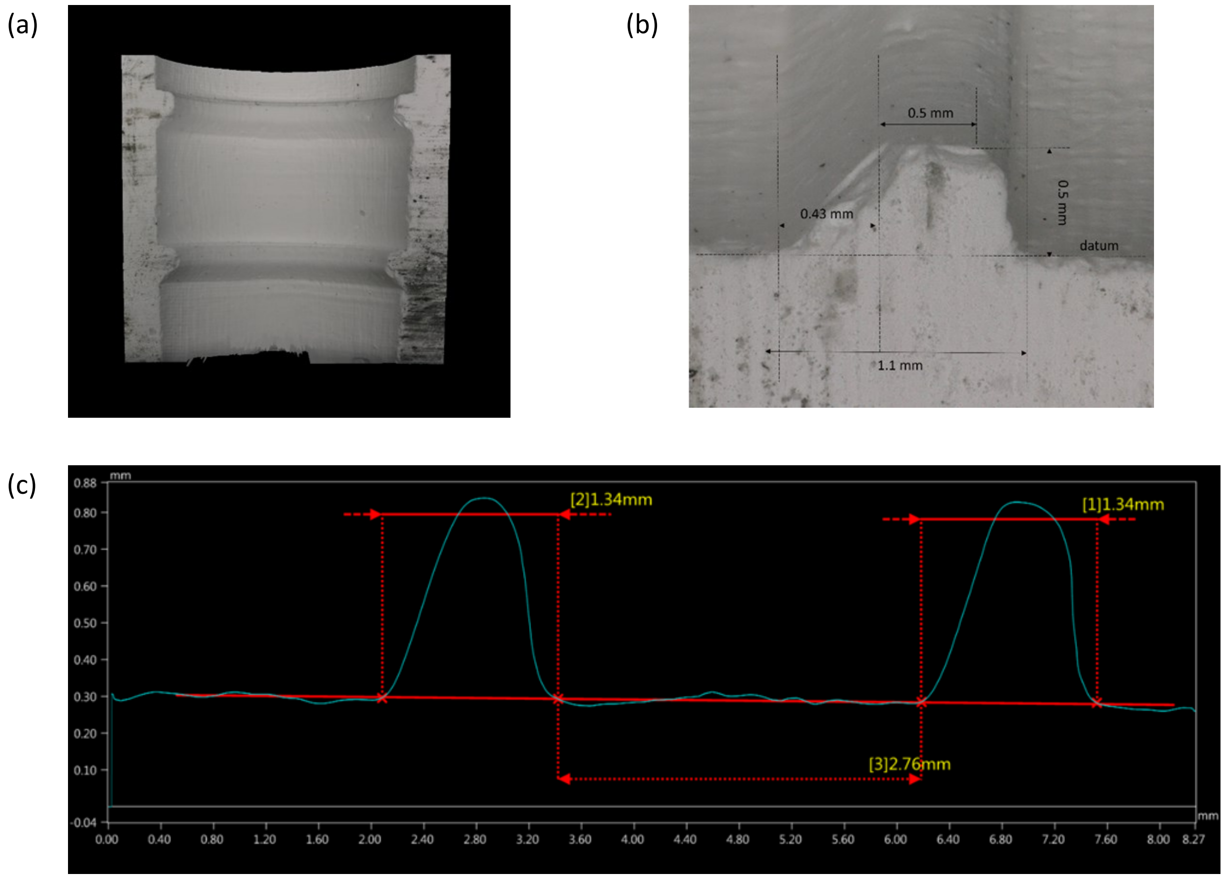

Figure 4. Geometry of the patterned membrane: (a) image of the inner surface of the membrane cutout. (b) and (c): Characteristic sizes of roughness elements.

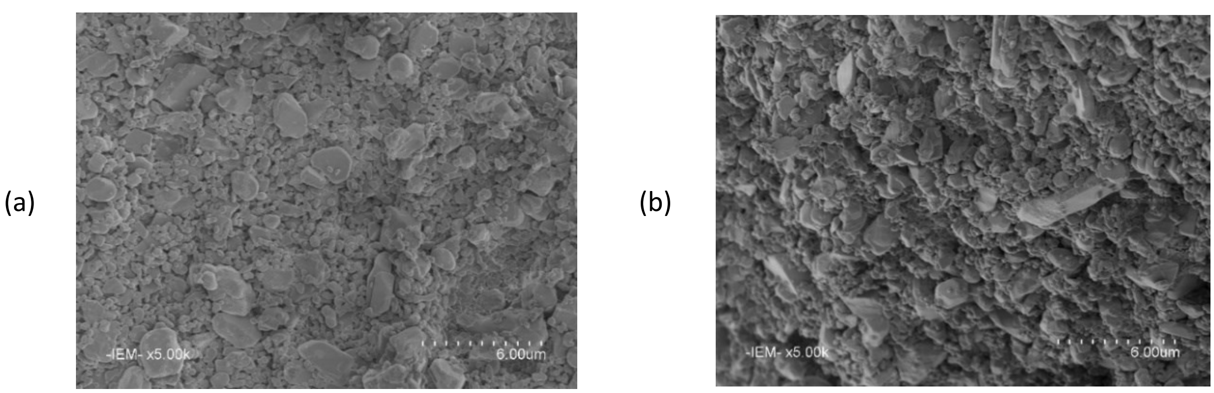

Figure 5. SEM images of the membrane: (a) planar surface and (b) cross section views.

Mercury porosimetry measurements yielded the porosity of ~ 33 % and the specific surface area of ~ 2.5 $m^2 g^{-1}$. These values are consistent with what can be expected to result from the limited sintering of a random close-packing arrangement of powder particles. The pore size distribution (Figure 6) is centered around an average pore size of ~ 0.2 µm. The prepared membranes can thus be classified as microfilters. Considering the implemented process of additive manufacturing, (stereolithography), no specific microstructural changes were expected neither for smooth nor for patterned membranes. This was experimentally confirmed in SEM observations of membrane cross-sections.

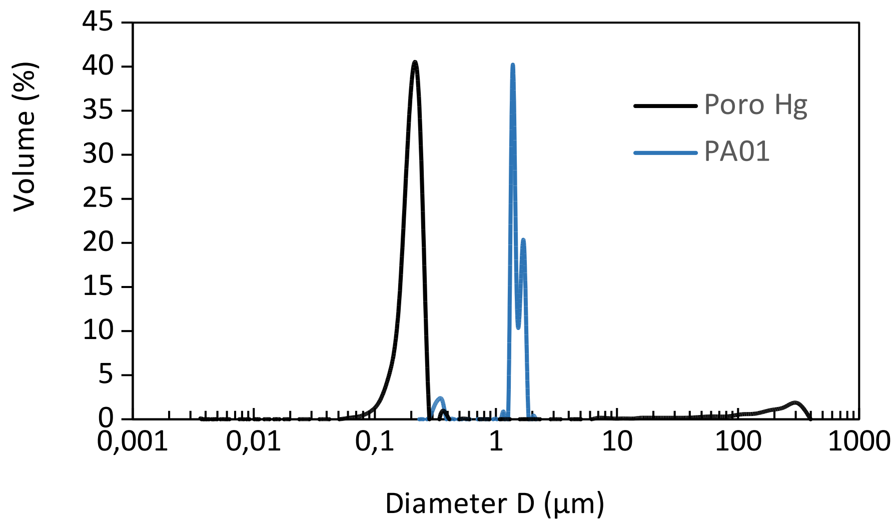

Figure 6. Pore size distribution of ceramic membranes and the size distribution of P. aeruginosa bacteria in the feed suspension.

4.3. Fouling experiments

Based on the DLS measurements, the average size of bacteria in the feed suspension was ~ 0.8 µm, which is significantly larger than the measured average pore size (~ 0.2 µm) of the membrane (Figure 6). The DLS measurements estimated the diffusion coefficient, which was then converted to particle size assuming that the scatterers are spherical.

Application of the Carman-Kozeny relation to mercury porosimetry data [28] estimates the intrinsic permeability of the membrane to be ~ 1.6 10^{-16} m^2. The expected water permeability at 23 °C is thus equal to 42 ± 16 $L \cdot m^{-2} \cdot h^{-1} \cdot bar^{-1}$, which is within the experimental error from the valued measured experimentally for a smooth membrane (69 ± 15 $L \cdot m^{-2} \cdot h^{-1} \cdot bar^{-1}$). The difference of filtering area for the patterned membranes was estimated to be the increase of 11.5 %, assuming an ideal geometry. The water permeability experimentally measured for such a patterned membrane, and taking into account the patterning effect on the filtering area, is 76 ± 13 $L \cdot m^{-2} \cdot h^{-1} \cdot bar^{-1}$. This is very close to the value measured for the smooth membrane. However, it must be noted that the average thickness of the two membranes is not exactly the same. An increase of 6.5 % was estimated for the patterned one (1.6 mm rather than 1.5 mm for the smooth one). This is discussed in the Supplementary Information (SI), section S3.

The results obtained in crossflow filtration tests are summarized in Figure 7. Based on the application of Hermia blocking law analysis to dead end filtration data (see SI, Figures S3 and S4), two fouling regimes could be discerned: pore blockage and cake filtration. The presence of integrated rings had no effect on pore blockage but led to a significant mitigation of fouling in the cake filtration regime at the higher value of crossflow velocity (Figure 7b). This is in good agreement with the numerical simulations and a mean value of turbulent dissipation rate at the surface of the membrane between the rings being much larger for the patterned membranes.

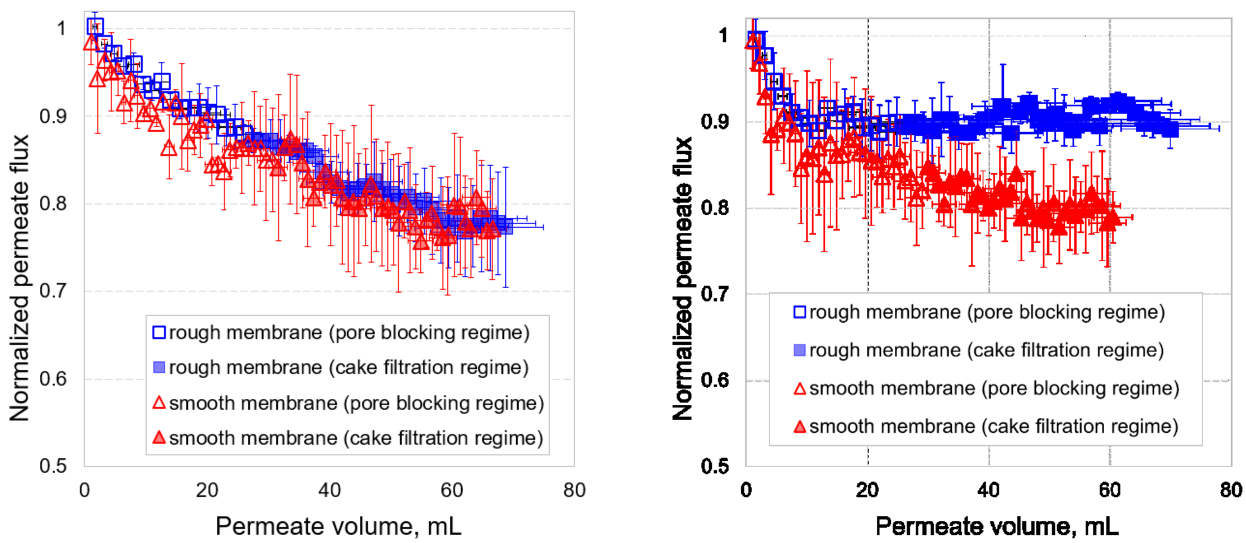

(a) *(b)*

Figure 7. Normalized permeate flux recorded in crossflow filtration tests with P. aeruginosa suspension as the feed and using *smooth and patterned membranes. (a) a crossflow velocity of 0.45 m·s^{-1}; (b) and a crossflow velocity of 0.68 m·s^{-1}. Empty symbols correspond to the filtration stage where fouling is due to pore blocking while filled symbols correspond to the cake filtration regime.*

4.4. Considerations of scale

The fouling tests revealed a significant difference in roughness-induced mitigation of fouling between the two studied crossflow velocities. For a crossflow velocity of 0.45 m·s^{-1}, the smooth and patterned membranes seem to be affected by fouling phenomena in a similar way. For both membrane types, the permeate flux decreased by ~ 22 % after 70 mL of permeate was collected. By contrast, significant differences were observed in tests with the crossflow velocity of 0.68 m·s^{-1}; in this case, whereas the smooth membranes exhibit the same 22 % flux decrease, the flux decline was only 10 % in experiments with the patterned filter. This result was very encouraging and provided the proof of concept of the patterned membranes.

Near the membrane surface, we calculated the mean value of the dissipation rate of the turbulent kinetic energy in the zone between two rings ($\varepsilon_{mean\_betw\_rings}$, cf. Table 2). We compared this value to the maximum value of ε localized just above the rings ($\varepsilon_{max\_above\_rings}$) and in both zones, we observed that the dissipation rate of the turbulent kinetic energy (ε) is multiplied by a factor 3.5 when the velocity is increase from 0.45 and 0.68 $m{\cdot}s^{-1}$. $\varepsilon_{mean\_betw\_rings}$ is close to 3.2 $m^2{\cdot}s^{-3}$ for v_{in}= 0.45 $m{\cdot}s^{-1}$ and 10.5 $m^2{\cdot}s^{-3}$ for v_{in}= 0.68 $m{\cdot}s^{-1}$, respectively (Table 2). Near the upper part of the rings, where the turbulence is the highest, $\varepsilon_{max\_above\_rings}$ is multiplied by a factor 5 when increasing the velocity (60 vs 300 $m^2{\cdot}s^{-3}$). The values of the Kolmogorov microscale, κ, are calculated using eq. (3) [29-31] and reported in Table 2.

$$\kappa = \left[\frac{\eta^3}{\varepsilon}\right]^{1/4} \tag{3}$$

Whatever the location (between the rings corresponding to the lowest values of ε, or near the upper part of the rings corresponding to the highest values of ε), κ increases 150 % with a decrease in the mean velocity from 0.68 to 0.45 $m{\cdot}s^{-1}$.

Table 2. Kolmogorov microscale κ in low ε and high ε zones in the vicinity of the membrane surface for two values of the average crossflow velocity.

Location along the membrane surface	Mean crossflow velocity, v_{in} ($m{\cdot}s^{-1}$)	Turbulent energy dissipation rate, ε ($m^2{\cdot}s^{-3}$)	Kolmogorov microscale, κ (μm)
Mean value between the rings $\varepsilon_{mean\_betw\_rings}$ 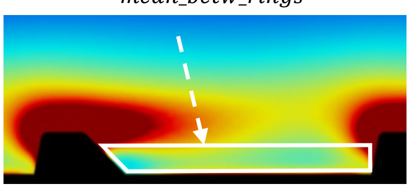	0.45	3.2	23.6
	0.68	10.5	17.6
Local value above the ring $\varepsilon_{max\_above\_rings}$ 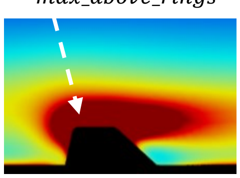	0.45	60	11.4
	0.68	300	7.6

Kolmogorov microscale corresponds to the lowest scale of turbulence where viscosity dominates and the turbulent kinetic energy is dissipated. So, κ is often a relevant hydrodynamic parameter, which could be linked to fouling mechanisms. As shown in Table 2, the values of κ are approximately two orders of magnitude smaller than characteristic dimensions of roughness features on the membrane surface where the size of the rings or the inter-ring distance are on the order of several millimeters (Figures 4b and 4c). We tentatively attribute the improvement in permeate flux (Figure 7b) to the disruption of the filter cake growth at the scale on several microns (i. e. ~ κ µm). Even if the fouling mechanisms are complex and their mitigation could be linked to several phenomena, the significant increase of the dissipation rate of the turbulent kinetic energy and the associated decrease of the Kolmogorov microscale are in good agreement with the fouling results reported in Figure 7.

4.5. Potential of stereolithography for ceramic membrane design

Through creating desired surface morphology at the mesoscale, additive manufacturing methods help control flow to mitigate deposition of colloids and larger particle and, thereby, mitigate membrane fouling. However, the methods impose limitations on the material properties of the membrane that supports such surface features. First, small alumina particle size helps improving both the spatial resolution of the stereolithography method and the mechanical properties of membranes post-sintering; however, the smaller size of the primary particles leads to a low final pore size. The pore diameter of ~ 0.2 µm reported in this work is more than an order of magnitude smaller than the pore size achievable by extrusion of pastes formulated from coarser and monodispersed powders. Addition of pore-forming agents in the stereolithography formulation is thus recommended to increase the pore size and achieve a better balance between resolution and permeability. Second, symmetrical patterned microfiltration membranes could be used as a porous support for the production of patterned ultrafiltration or nanofiltration membranes by deposition of successive thin layers by slip casting.

5. Conclusions

CFD simulations were successfully used for guiding the design of 3D-printed tubular single-channel ceramic membranes and optimizing the surface morphology at the mesoscale in order to improve the hydrodynamic control of membrane fouling. CFD predictions were corroborated by the experimental data on membrane fouling. The mesoscale design of microfiltration membranes by additive manufacturing can be combined with preparing the lower porosity separation layer by conventional methods of separation layer. Such optimal combination of membrane fabrication methods may be practically implemented through a multistep/multi-method morphological design as an alternative to changing the casting mixture composition for pore size control.

Acknowledgments

We are grateful to Mr. Didier Cot and Dr. Martin Drobek (both at Institut Européen des Membranes) for performing SEM and Hg porosimetry analyses, respectively. We also thank 3DCERAM SINTO (Limoges, France) for the manufacturing the prototype membranes and providing them to our team. This material is based upon work supported in part by the U.S. National Science Foundation under grant No. OISE-1952438, which supported the cooperation between Institut Européen des Membranes and Michigan State University.

References

[1] T. Chartier, A. Badev, Rapid Prototyping of Ceramics, in: S. Somiya, M. Kaneno (Eds.) Handbook of Advanced Ceramics, 2013, pp. 489-524.

[2] T. Chartier, C. Dupas, M. Lasgorceix, J.D.N. Brie, C. Chaput, Additive manufacturing to produce complex 3D ceramic parts, J. Ceram. Sci. Technol., 6 (2014) 95-104.

[3] Z. Chen, Z. Li, J. Li, C. Liu, C. Lao, Y. Fu, C. Liu, Y. Li, P. Wang, Y. He, 3D printing of ceramics: A review, J. Eur. Ceram. Soc., 39 (2019) 661-687.

[4] T. Chen, D. Wang, X. Chen, M. Qiu, Y. Fan, Three-dimensional printing of high-flux ceramic membranes with an asymmetric structure via digital light processing, Ceram. Int., 48 (2022) 304-312.

[5] H. Dommati, S.S. Ray, J.-C. Wang, S.-S. Chen, A comprehensive review of recent developments in 3D printing technique for ceramic membrane fabrication for water purification, RSC Adv., 9 (2019) 16869.

[6] D. Wang, T. Chen, Y. Zeng, X. Chen, W. Xing, Y. Fan, X. Qiao, Optimization of UV-curable alumina suspension for digital light processing of ceramic membranes, J. Memr. Sci., 643 (2022).

[7] H.A. Balogun, R. Sulaiman, S.S. Marzouk, A. Giwa, S.W. Hasan, 3D printing and surface imprinting technologies for water treatment: A review, J. Water Process. Eng., 31 (2019) 100786.

[8] T. Femmer, A. Kuehne, J. Torres-Rendon, A. Walther, M. Wessling, A.J. Kuehne, Print your membrane: Rapid prototyping of complex 3D-PDMS membranes via a sacrificial resist, J. Memr. Sci., 478 (2015) 12-18.

[9] M.N. Issac, B. Kandasubramanian, Review of manufacturing three-dimensional-printed membranes for water treatment, Environ. Sci. Pollut.. Res., 27 (2020) 36091-36108.

[10] J.-Y. Lee, W.S. Tan, J. An, C.K. Chua, C.Y. Tang, A.G. Fane, T.H. Chong, The potential to enhance membrane module design with 3D printing technology, J. Memr. Sci., 499 (2016) 480-490.

[11] Z.-X. Low, Y.T. Chua, B.M. Ray, D. Mattia, I.S. Metclafe, D.A. Patterson, Perspective on 3D printing of separation membranes and comparison to related unconventional fabrication techniques, J. Memr. Sci., 523 (2017) 596-613.

[12] W. Choi, C. Lee, D. Lee, Y.J. Won, G.W. Lee, M.G. Shin, B. Chun, T.-S. Kim, H.D. Park, H.W. Jung, J.S. Lee, J.-H. Lee, Sharkskin-mimetic desalination membranes with ultralow biofouling, J. Mater. Chem. A, 6 (2018) 23034-23045.

[13] Y.-J. Won, S.-Y. Jung, J.-H. Jang, J.-W. Lee, H.-R. Chae, D.-C. Choi, K.H. Ahn, C.-H. Lee, P.-K. Park, Correlation of membrane fouling with topography of patterned membranes for water treatment, J. Memr. Sci., 498 (2016) 14-19.

[14] Z. Zhao, A. Ilyas, K. Muylaert, I.F. Vankelecom, Optimization of patterned polysulfone membranes for microalgae harvesting, Bioresource Technol., 309 (2020).

[15] Z. Lyu, T.C.A. Ng, T. Tran-Duc, G.J.H. Lim, Q. Gu, L. Zhang, Z. Zhang, J. Ding, N. Phan-Thien, J. Wang, H.Y. Ng, 3D-printed surface-patterned ceramic membrane with enhanced performance in crossflow filtration, J. Memr. Sci., 606 (2020) 118138.

[16] T.C.A. Ng, Z. Lyu, C. Wang, S. Guo, W. Poh, Q. Gu, L. Zhang, J. Wang, H.Y. Ng, Effect of surface-patterned topographies of ceramic membranes on the filtration of activated sludge and their interaction with different particle sizes, J. Memr. Sci., 645 (2022).

[17] Z. Yang, J. Cheng, C. Yang, B. Liang, CFD-based optimization and design of multi-channel inorganic membrane tubes, Chin. J. Chem. Eng., 24 (2016) 1375-1385.

[18] L. Broussous, P. Schmitz, E. Prouzet, L. Becque, A. Larbot, New ceramic membranes designed for crossflow filtration enhancement, Separ. Purif. Technol., 25 (2001) 333-339.

[19] P.A. Lescoch, J., Game changer in inorganic membranes, in: ICIM 2018, Dresden, 2018.

[20] S.M. Ali, A. Qamar, S. Phuntsho, N. Ghaffour, J.S. Vrouwenvelder, H.K. Shon, Conceptual design of a dynamic turbospacer for efficient low pressure membrane filtration, Desalination, 496 (2020).

[21] K. Guerra, J. Pellegrino, Development of a techno-economic model to compare ceramic and polymeric membranes, Separ. Sci. Technol., 48 (2013) 51-65.

[22] B.E. Launder, D.B. Spalding, The numerical computation of turbulent flows, Comput. Method. Appl. Mechanics Eng., 3 (1974) 269-289.

[23] W.P. Jones, B.E. Launder, The prediction of laminarization with a two-equation model of turbulence, Int. J. Heat Mass Transfer, 15 (1972) 301-314.

[24] B.H. Iglewski, Pseudomonas, in: S. Baron (Ed.) Medical Microbiology, University of Texas Medical Branch at Galveston, Galveston, TX, 1996.

[25] A. Einstein, A New Determination of Molecular Dimensions, Ann. Physik, 34 (1911) 591.

[26] M. Herzberg, M. Elimelech, Biofouling of reverse osmosis membranes: Role of biofilm-enhanced osmotic pressure, J. Memr. Sci., 295 (2007) 11-20.

[27] F. Wang, V.V. Tarabara, Pore blocking mechanisms during early stages of membrane fouling by colloids, J. Colloid Interface Sci., 328 (2008) 464-469.

[28] C.J. Brinker, Scherer, G. W., Sol-Gel Science: The Physics and Chemistry of Sol-Gel Processing, 1990.

[29] A.N. Kolmogorov, The local structure of turbulence in incompressible viscous fluid for very large Reynolds numbers, Dokl. Akad. Nauk. SSSR, 30 (1941) 299-303.

[30] A.N. Kolmogorov, The local structure of turbulence in incompressible viscous liquid, Dokl. Akad. Nauk. SSSR, 31 (1941) 538-541.

[31] A.N. Kolmogorov, Dissipation of energy in locally isotropic turbulence, Dokl. Akad. Nauk. SSSR, 32 (1941) 19-21.

Supplementary information

for the manuscript

CFD-guided patterning of tubular ceramic membrane surface by stereolithograhy: Optimizing morphology at the mesoscale for improved hydrodynamic control of membrane fouling

Cyril Chevarin[1], Xunhao Wang[2], Denis Bouyer[1*], Volodymyr V. Tarabara[2**], Thierry Chartier[3], André Ayral[1]

[1] Institut Européen des Membranes IEM – UMR 5635, ENSCM, CNRS, Univ Montpellier, Montpellier, France
[2] Department of Civil and Environmental Engineering, Michigan State University, East Lansing, MI 48824, USA
[3] CNRS, University of Limoges, Institute of Research for Ceramics (IRCER), UMR 7315, European Ceramics Center, Limoges, France

S1. k-ε turbulence model

To take into account turbulence effect, the standard k-ε turbulence model[1] as used. This model is robust, accuracy and widely used for many flow applications.

In addition to the conservation of momentum equation in the Navier-Stokes equation (Eq. (1)), the standard k-ε turbulence model, which is a semi-empirical model, is based on two additional transport equations for the turbulent kinetic energy k and for the turbulent dissipation rate ε as follow:

For the turbulent kinetic energy k (in $m^2.s^{-2}$):

$$\rho(\vec{v}.\nabla k) = \nabla.\left(\left(\eta + \frac{\eta_t}{\sigma_k}\right)\nabla k\right) + P_k - \rho\epsilon \qquad \text{(A1)}$$

where P_k is the productive term of k due to the mean velocity gradients

$$P_k = \eta_t\left[\nabla\vec{v}\colon(\nabla\vec{v} + \nabla\vec{v}^T) - \frac{2}{3}(\nabla.\vec{v})^2\right] - \frac{2}{3}\rho k\nabla.\vec{v} \qquad \text{(A2)}$$

And for the turbulent dissipation rate ε (in $m^2.s^{-3}$):

$$\rho(\vec{v}.\nabla\varepsilon) = \nabla.\left(\left(\eta + \frac{\eta_t}{\sigma_\varepsilon}\right)\nabla\varepsilon\right) + C_{\varepsilon 1}\frac{\varepsilon}{k}P_k - C_{\varepsilon 1}\rho\frac{\varepsilon^2}{k} \qquad \text{(A3)}$$

[1] B.E. Launder, D.B. Spalding, The numerical computation of turbulent flows, Comput. Method. Appl. Mechanics Eng., 3 (1974) 269-289.

In this k-ε model, the turbulent viscosity η_t ((in m².s^{-2}) was modeled by combining k and ε using the equation:

$$\eta_t = \rho C_\eta \frac{k^2}{\varepsilon} \tag{A4}$$

The standard k-ε model constants $C_{\varepsilon 1}$, $C_{\varepsilon 2}$, C_η, σ_k and σ_ε were issued from experimental data and could be adjusted. The default value of these constants are listed in Table S1.

Table S1. Model constants.

Constant	$C_{\varepsilon 1}$	$C_{\varepsilon 2}$	C_η	σ_k	σ_ε
Value	1.44	1.92	0.09	1.0	1.3

S2. Preparation of bacteria stock

To prepare the bacteria stock, one liter of PA01 (late exponential growth phase) with a final optical density (600 nm) of 1 were washed twice with 150 mM NaCl, (centrifuged for 10 min at 8000 rpm and 4 °C and resuspended by vortexing) and incubated in 4% formaldehyde solution for 2 h at room temperature to fix the bacteria. The cells were then washed three times with 150 mM NaCl (centrifuged for 10 min at 8000 rpm and 4 ℃, and resuspended by vortexing) [20]. The fixed bacteria stock (pH 6) was stored at 4 °C for subsequent use.

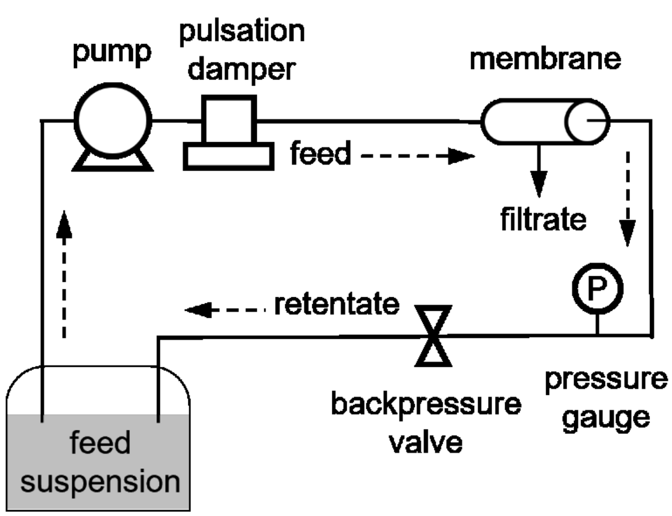

Figure S1. Schematic of the crossflow filtration setup. Dead-end filtration tests were performed using the same system but with the retentate outlet closed.

S3. Comparison of water permeability values for smooth and patterned membranes

Because the thickness of the two types of membranes is not exactly the same (average thickness of 1.5 mm for the smooth ones versus 1.6 mm for the patterned ones), their measured water permeabilities cannot be compared directly. Referring to the terminology used for gas permeation, the water permeability corresponding to the water flux divided by the transmembrane pressure should rather be named water permeance. Considering that such symmetric membranes are made with the same and homogeneous membrane material, it is here recommended to rather compare the values of "coefficient of permeability for water in the membrane material". It is equal to the water flux divided by the pressure gradient across the membrane. It can thus be calculated by multiplying the water permeability by the membrane thickness. The obtained values are as follows:

Value calculated from the microstructure data: 63 ± 23 $L.mm \cdot m^{-2} \cdot h^{-1} \cdot bar^{-1}$

Value measured with a smooth membrane: 104 ± 23 $L.mm \cdot m^{-2} \cdot h^{-1} \cdot bar^{-1}$

Value measure with a patterned membrane: 122 ± 22 $L.mm \cdot m^{-2} \cdot h^{-1} \cdot bar^{-1}$

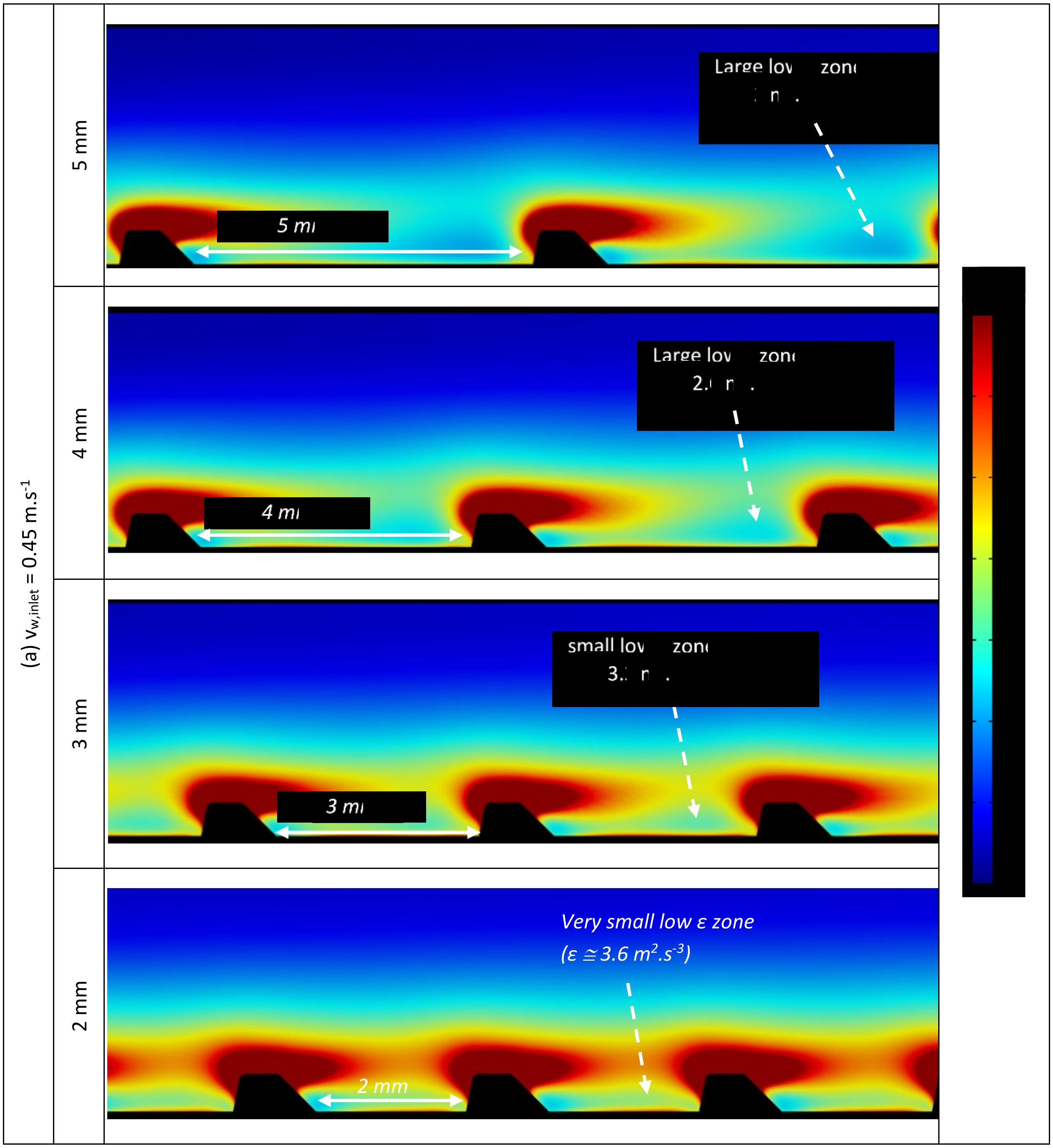
(a) $v_{w,inlet}$ = 0.45 m.s^{-1}
5 mm
[redacted]
[redacted]
4 mm
[redacted]
[redacted]
3 mm
[redacted]
[redacted]
2 mm
Very small low ε zone
($\varepsilon \simeq 3.6\ m^2.s^{-3}$)
2 mm
[redacted]

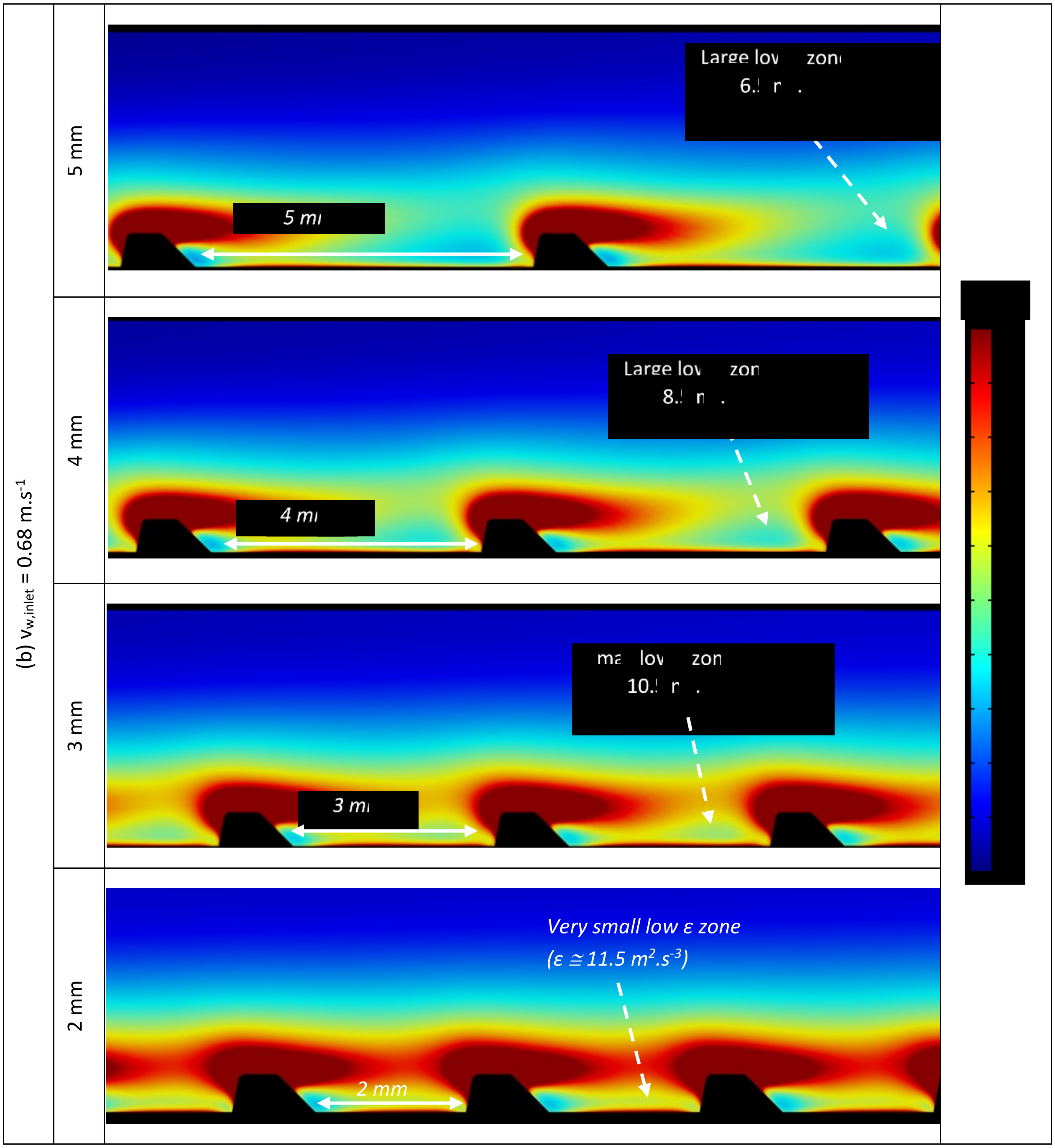

Figure S2. Mapping of ε inside the tubular membrane for four different distances between the rings (2, 3, 4 and 5 mm) and the two explored values of v_{inlet} : (a) 0.45 m s^{-1}; (b) 0.68 m s^{-1}.

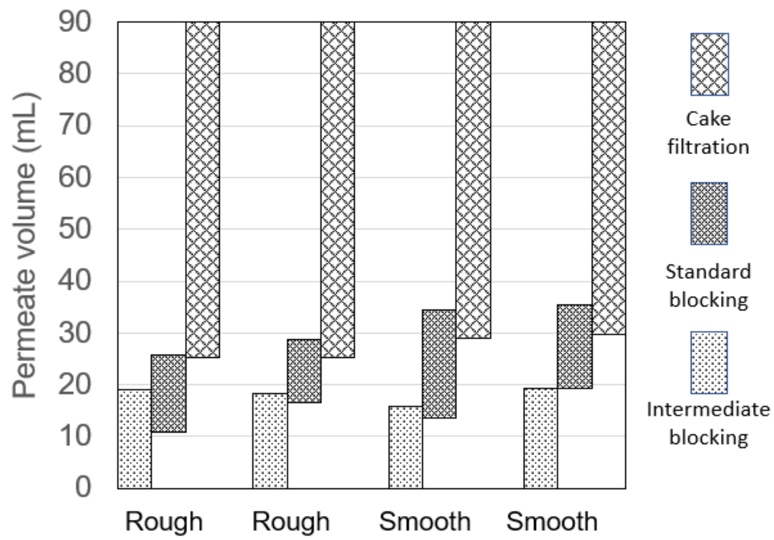

Figure S3. Evolution of fouling mechanism during dead-end filtration of bacterial suspensions by smooth and rough membranes.

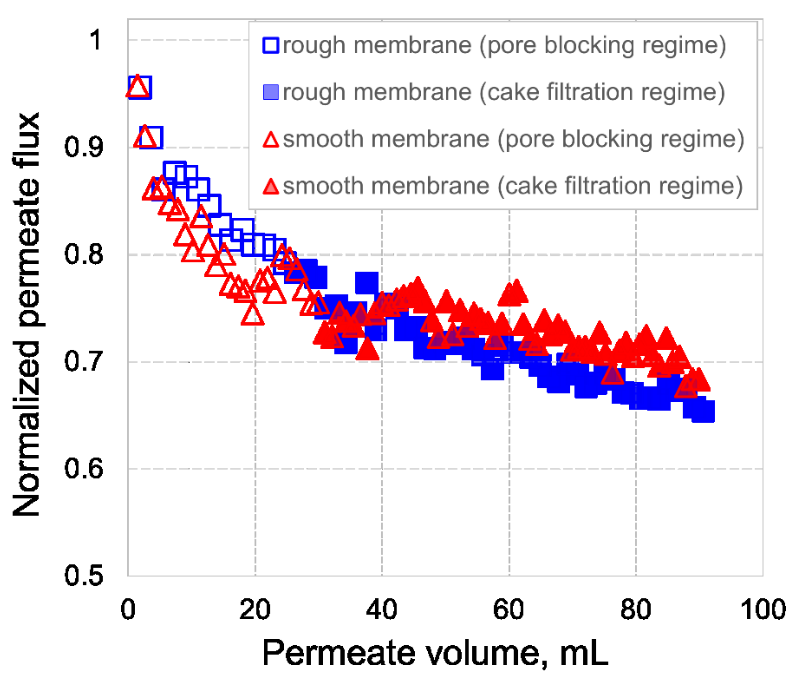

Figure S4. Normalized permeate flux recorded in dead-end filtration tests with smooth and rough membranes.